



Progress of Design and Development for the ITER Radial Neutron Camera

B. Esposito¹ · D. Marocco¹ · G. Gandolfo¹ · F. Belli¹ · L. Bertalot¹² · J. Blocki² · D. Bocian² · G. Brolatti¹ · M. Cecconello⁸ · C. Centioli¹ · R. C. Pereira⁷ · S. Conroy⁸ · F. Crescenzi¹ · N. Cruz⁷ · L. de Bilbao¹⁰ · A. Domenicone¹ · Q. Ducasse¹⁷ · G. Di Mambro^{4,15} · D. Dongiovanni¹ · I. Eletxigerra¹¹ · B. Etxeita¹¹ · A. Fernandez⁷ · O. Ficker⁹ · P. Gallina¹³ · T. Giacomini¹² · G. Ginoulhiac¹ · J. Godlewski² · A. Hjalmarsson⁸ · M. Imrisek⁹ · R. Kantor² · K. Kasprzak² · J. Kotula² · V. Krasilnikov¹² · M. Lewandowska² · A. Maffucci^{4,15} · U. Marotta¹ · D. Marzullo¹³ · G. Mazzitelli¹ · G. Mazzone¹ · R. Miklaszewski⁶ · K. Mikszuta-Michalik⁶ · W. Maciocha² · S. Magagnino¹ · M. Misano¹ · J. Mlynar⁹ · C. Monti¹ · F. Moro¹ · R. Ortwein² · M. Passeri^{1,5} · T. Pinna¹ · E. Pirovano³ · V. Pisciotta¹ · F. Pompili¹ · S. Podda¹ · M. Riva¹ · B. Santos⁷ · J. Sousa⁷ · J. Swierblewski² · P. Szklarz² · A. Tati¹⁴ · S. Ventre^{4,15} · F. Villone^{4,16} · N. Virgili¹ · A. Zimbal³

Accepted: 18 July 2022 / Published online: 18 September 2022
© The Author(s) 2022

Abstract

The paper presents an overview of the design status of the Radial Neutron Camera (RNC), that, together with the Vertical Neutron Camera, will provide, through reconstruction techniques applied to the measured line-integrated neutron fluxes, the time resolved measurement of the ITER neutron and α -source profile (i.e. neutron emissivity, neutrons emitted per unit time and volume). The RNC is composed of two subsystems, the In-Port RNC and Ex-Port RNC located, respectively, inside and outside the Plug of Equatorial Port #01. The In-Port subsystem is in a more advanced design stage since it has recently undergone the Final Design Review in the ITER procurement process. The paper describes the diagnostic layout, the interfaces, the measurement capabilities and the main challenges in its realization. Prototyping and testing of neutron detectors and electronics components were carried out and led to the choice of the component solutions that can match the environmental and operational constraints in terms radiation hardness, high temperature and electromagnetic compatibility. The performance of the RNC in terms of neutron emissivity measurement capability was assessed through 1D and 2D reconstruction analysis. It is proven that the neutron emissivity can be reconstructed in real-time within the measurement requirements: 10% accuracy, 10 ms time resolution and $a/10$ (a = plasma minor radius) space resolution.

Keywords Neutron detector · Neutron camera · Tomography · ITER

Introduction

The time resolved measurement of the neutron and α -source profile (i.e. *neutron emissivity*, neutrons emitted per unit time and volume ($s^{-1} m^{-3}$)) and the associated *fusion power density* is provided in ITER by two separate

diagnostic systems [1], the Radial Neutron Camera (RNC) and the Vertical Neutron Camera (VNC), located in different sectors of the machine. Both systems exploit collimated Lines of Sight (LoS) along which uncollided 14 MeV and 2.5 MeV line-integrated neutron fluxes from deuterium–tritium (DT) and deuterium–deuterium (DD) fusion reactions are measured. Such fluxes are processed, through reconstruction techniques, for the primary function of providing in real-time the neutron emissivity over a poloidal cross section of the plasma, to be used for fusion power control purposes.

The combination of RNC and VNC data will enable a full 2D tomographic reconstruction of the neutron

Disclaimer F4E: This publication reflects only the views of the authors, Fusion for Energy cannot be held responsible for any use of the information contained therein. ITER: The views and opinions expressed herein do not necessarily reflect those of the ITER Organization.

Extended author information available on the last page of the article

emissivity. Moreover, it will provide also information on other quantities, namely, the core ion temperature profile (T_i) and the fuel ratio profile (n_D/n_T) and will also monitor any spatial asymmetries in the fusion power as well as shifts of the plasma position [2].

This paper deals with the progress of the design and development carried out for the RNC. An overview of earlier work on the RNC design is provided in [3], while details on the status of the VNC design can be found elsewhere [1, 4].

The RNC is located in the ITER Equatorial Port #01 and is composed by two collimating structures, the first one, (In-Port RNC, probing the outer plasma) located inside the region of the port (Port Plug) within the tokamak vessel vacuum and the second one (Ex-Port RNC, probing the inner plasma) placed outside such region. Both structures view the plasma radially through vertical slots in the Diagnostic Shielding Module of the Port Plug.

A design process model based on system engineering has been adopted, leading to a qualitative and quantitative methodology for the identification of the RNC baseline architecture [5]. The In-Port RNC is in a more advanced design stage since it has recently undergone (end 2021) the Final Design Review in the ITER procurement process while the Preliminary Design Review for the Ex-Port subsystem is foreseen in early 2023. A global overview of the RNC design as well of its main interfaces is provided in Chapter 2.

The main challenges for the realization of the RNC concern the Diagnostic Performance and the R&D and Prototype Testing that are treated, respectively, in Chapter 3 and Chapter 4. The assessment of the performance of the RNC has been made in terms of the capability of reconstructing the neutron emissivity in real-time with the requested time resolution of 10 ms. The R&D and Prototype Testing is carried out in order to enable some critical components to reach a sufficient level of development that guarantees implementation in the ITER environment. More specifically, the R&D and testing campaign has focused on (a) the resistance of the In-Port RNC neutron detectors to the environmental/operational conditions; (b) the development of electrical feedthroughs for the primary/secondary vacuum interface in the In-Port RNC; (c) the electromagnetic compatibility assessment of the electronic chain; (d) the development of a novel pressurized ^4He scintillator detector for the Ex-Port RNC.

The final section of the paper (Chapter 5) deals with the prospects for the ITER RNC procurement based on the design and R&D.

RNC Design Overview

A well-defined volume has been allocated by the Port Integrator in the Port Plug, the Port Interspace and Port Cell to accommodate the RNC high level components, defined as Embarked Units (*EU*). An *EU* is a Part of the Diagnostic that makes sense to be treated separately to organize the integration, either for technical or management reasons at design, manufacturing, installation, testing, or commissioning phases. Figure 1 shows the plasma coverage of the RNC and an overview of the various RNC *EUs*. Two cabinets located in the Port Cell are also associated to the diagnostic: (a) *EU21*, containing the front-end electronics (Preamplifiers) for the whole RNC; (b) *EU22*, containing the RNC Service Vacuum System components and the RNC Cooling components.

MCNP Monte Carlo code analysis has been extensively used [6] in order to optimize the RNC design by enhancing the diagnostic measurement performance and by evaluating the nuclear loads to be withstood by its structural elements, detectors and associated components. A calibration procedure has been defined that relies on embedded sources, reference ITER pulses and cross-calibration with ITER fission chamber monitors and activation system coupled to Monte Carlo simulations of radiation transport [7].

In-PORT RNC

The In-Port RNC, located in one of the three parallel modules of the Port Plug (*Drawer #3*), is devoted to probe the edge of the plasma ($r/a > 0.67$). It has 6 LoS, with detectors located in a Cassette Assembly (3 detector modules in the upper part of the cassette and 3 detector modules in the Lower part of the cassette). The LoS traverse the Diagnostic Shielding Module (DSM) and reach the first wall. The LoS in the upper and lower parts of the Cassette are located in two parallel planes that are not exactly radial (thus not intersecting the machine axis). The two planes are 75 mm apart and the distance between the plane containing the Lower Cassette and the axis of the port is 371 mm.

The In-Port RNC is composed by the following *EUs* (Fig. 2):

- *EU02 DSM 3 Optical Path*: shaped conical voids within the DSM and the Diagnostic First Wall corresponding to each LoS.
- *EU04 Collimator Tubes*: parts of the Collimator units in *EU04* (one for each LoS) connected to the DSM and to the Cassette Assembly.
- *EU03 Cassette Assembly*: sealed container connected to the secondary vacuum system enclosing:

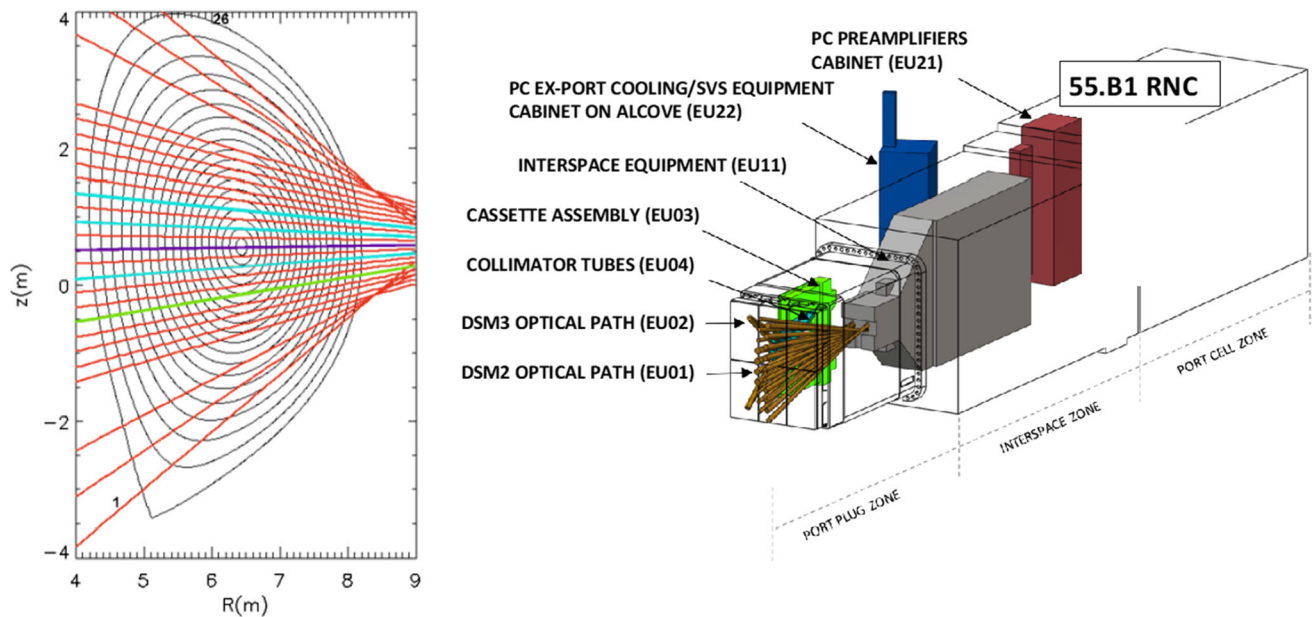


Fig. 1 Overview of the RNC LoS (left) and its Embarked Units (right)

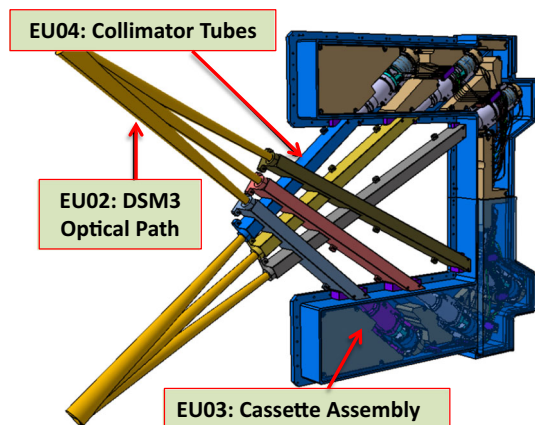


Fig. 2 In-Port RNC Embarked Units

- Parts of the Collimator units in *EU03*, one for each LoS.
- Detector Modules (3 units in the Upper part of Cassette Assembly and 3 units in the Lower part of the Cassette Assembly). Each Detector Module contains two in-line detectors: a single Crystal Diamond matrix (sCD) and a ^{238}U Fission Chamber (FC). Each detector is equipped with a thermocouple for temperature monitoring.
- Beam Dumps & shielding material. Sintered Boron Carbide modules providing neutron shielding and minimizing the rate of decay gammas.

Ex-Port RNC

The Ex-Port RNC, devoted to probe the core of the plasma ($r/a < 0.54$), consists of two *EUs* (Fig. 3):

- *EU11 IS Equipment*: located in the port interspace and containing the Flight Tubes, the Collimation Units, the Detector Modules, the Shielding Block and the Beam Dumps;
- *EU01 DSM 2 Optical Path*: located in the Port Plug in *Drawer #2* and containing the Optical Paths corresponding to the LoS.

The Ex-Port RNC has strong physical interfaces with two other diagnostics (Fig. 4): the High Resolution Neutron Spectrometer (HRNS) [8] and the Radial Gamma Ray Spectrometer (RGRS) [9] that feature dedicated LoS.

The Ex-Port RNC has 16 LoS distributed in two radial planes (i.e. intercepting the machine axis). The planes are separated in the toroidal direction by an angle of 1.414° ; the right and left planes have, respectively, angles of 0.8° and 0.62° with respect to the Port axis. The LoS of the two planes are interleaved, in that the second plane is obtained from the first one by a rigid rotation around the focus of 1.8° . The left plane has 10 RNC LoS while the right plane contains 6 RNC LoS since the four central LoS are exclusively used by RGRS and HRNS. *EU11* is provided with dedicated holes for the HRNS/ RGRS beam paths.

The HRNS features a single dedicated LoS with the central LoS on the right plane of the Ex-Port RNC. This LoS has exclusive HRNS use: no use of RNC detector is foreseen in such LoS.

Fig. 3 Ex-Port RNC Embarked Units

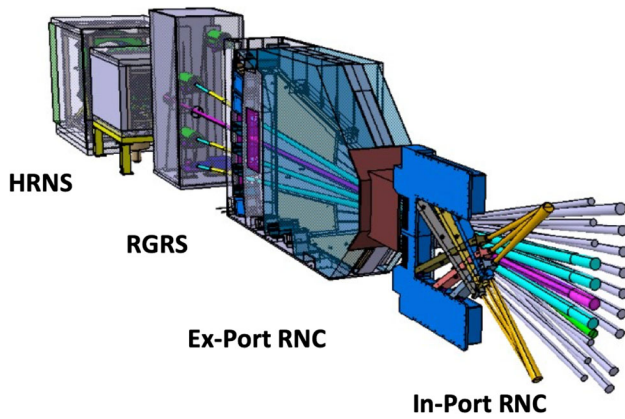
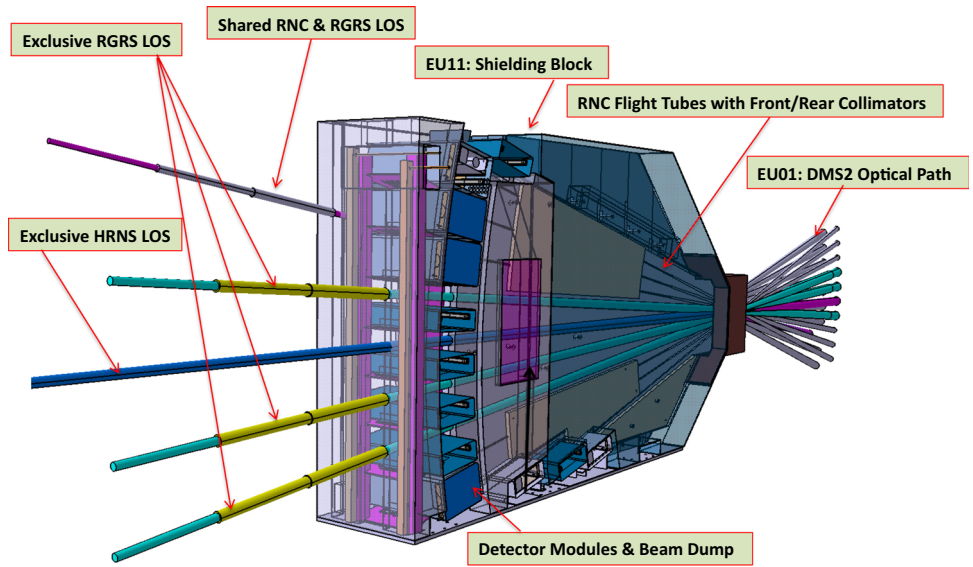


Fig. 4 RNC together with its interfacing diagnostics

The RGRS has total of 4 LoS for runaway electron and alpha measurements: 1 LoS is shared with the RNC on the left plane and 3 LoS for exclusive RGRS use are present on the right plane (no use of RNC detectors is foreseen in such exclusive LoS). All RGRS detectors will be mounted, behind the RNC detectors, in the Port Cell area.

The Port Plug closure plate (carrying out a confinement barrier safety function) has a surface with smaller thickness in correspondence of the Ex-Port LoS (*customization of the closure plate*) in order to minimize the attenuation of uncollided neutrons directed to the Ex-Port detectors.

Shielded Cabinet for Preamplifiers

The preamplifiers for RNC detectors need to be as close as possible to the detectors in order to minimize signal degradation. Their closest possible location is the Port Cell (~ 8.5 m distance from the In-Port RNC detector units) where, however, high radiation levels are present.

A shielded cabinet for preamplifiers (EU21) is, therefore, included in the design (Fig. 5), bolted on the Port Cell Supporting Structure. Protection of preamplifiers from fast and thermal neutrons, gamma radiation and electromagnetic fields, is achieved through a multi-layered structure: (a) B₄C layer to thermalize (moderate) fast neutrons by neutron scattering; (b) cadmium layer to absorb the thermalized neutrons by means of capture reactions; (c) tungsten layer to absorb the gammas (environmental and produced by capture reactions); (d) ferromagnetic material layer for electromagnetic shielding. A stainless steel armour encloses the various shielding layers. Its weight (7 tons) is the maximum that can be allocated based on the constraints posed by the Port Integrator. MCNP calculations indicate that this cabinet reduces the total absorbed dose to 3 Gy and the neutron flux to $7.2 \times 10^3 \text{ s}^{-1} \text{ cm}^{-2}$.

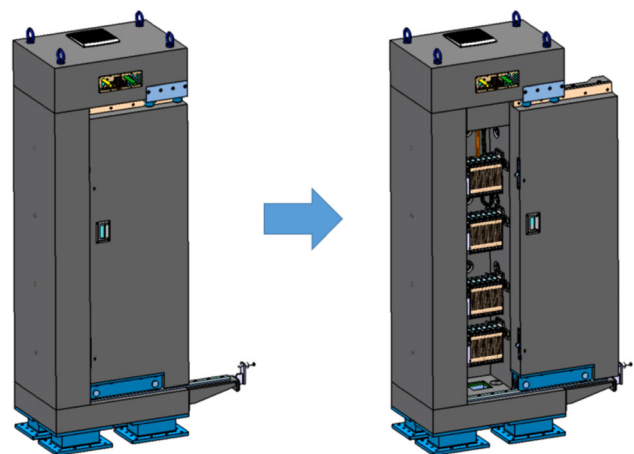


Fig. 5 EU21 Shielded Cabinet for preamplifiers

Table 1 Features of the RNC neutron detectors

Detector	Location	Shape	Thickness/ Amount	Diameter/Sensitive Area	Energy threshold (MeV)	14 MeV & 2.5 MeV efficiency (counts/neutron)
Plastic Scintillator	Ex-port plug	Cylinder	15 mm	15 mm	10 (DT), 1.8 (DD)	8×10^{-3} (DT), 3×10^{-2} (DD)
^4He Scintillator	Ex-port plug	Cylinder	30 mm	44 mm	6.2 (DT)	1.9×10^{-3}
Diamond	In-port plug	Matrix	50 μm /30 pixels	30 \times 0.4 mm \times 0.4 mm	7.5 (DT), 0.3 (DD) (deposited energy)	5×10^{-5} (DT), 0.1×10^{-2} (DD)
Fission chamber	In-port plug	Multilayer	145 mg ^{238}U	32 mm	–	5.4×10^{-5} (DT)

Detectors and Interfaces

The RNC neutron detectors, operated in pulse mode, are summarized in Table 1. There are 6 In-Port Detector Modules (Fig. 6), each one containing:

- One sCD matrix as main detector. This type of detector has a selectable energy threshold and has spectrometric capabilities. The matrix is needed in order to maximize the sensitive area.
- One ^{238}U FC as complementary detector. The FC has no 2.5/14 MeV discrimination capability and no selectable energy threshold. It also features a higher neutron background fraction.

Space constraints due to interfaces (maximum number of port plug feedthroughs) impose a limitation of a maximum of 2 signal cables per detector. For the sCD one triaxial mineral insulated cable per submatrix is used, while for the ^{238}U FC one mineral insulated cable is used for the anode and one for the cathode. Differential output is used for all detectors signals.

There are 16 Ex-Port Detector Modules (Fig. 7), each one containing:

- One gas scintillator (^4He) as main detector for full power DT measurements
- One plastic scintillator (EJ-276G, featuring n/γ discrimination) for low power DT measurements
- One sCD matrix as backup detector for full power DT measurements.

The RNC has interfaces not only, as seen above, with other diagnostics, but also with several ITER systems. Figure 8 provides an overview of all interfaces in the In-Port RNC: more details can be found in [10].

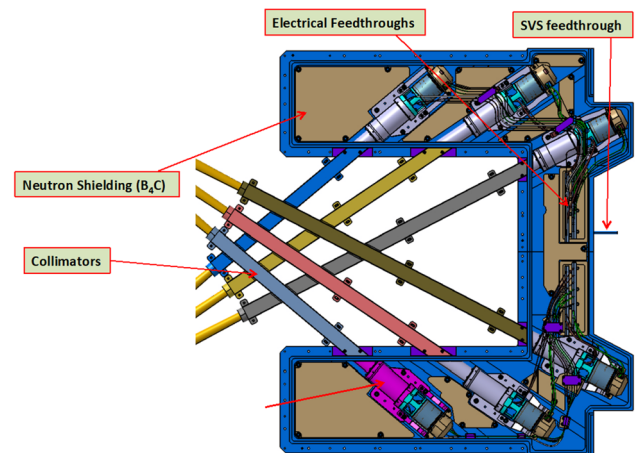


Fig. 6 In-Port RNC detector modules and other components inside the cassette assembly

Diagnostic Performance

The performance of the RNC has been assessed through 1D and 2D neutron emissivity reconstruction analysis. The 1D reconstruction code (Measurement Simulation Software Tool (MSST [3])) uses constant emissivity on magnetic flux surfaces and is based on Tikhonov regularization with first derivative objective functional [11, 12]. The 2D tomography code is based on the Minimum Fisher Regularization (MFR) method [13] and can include the total neutron yield value provided by an independent diagnostic as additional constraint in the tomography procedure [14].

The neutron fluxes at the detector positions as well as the expected uncollided neutrons count rates (above selected detectors energy thresholds) used as input for the analysis are shown in Fig. 9. The two codes were used to reconstruct the DT Q = 10 scenario (neutron yield of $1.8 \times 10^{20} \text{ s}^{-1}$) with 10 ms time resolution: 100 synthetic datasets were used in the MFR case and 1000 in the MSST case. The analysis was carried out considering only

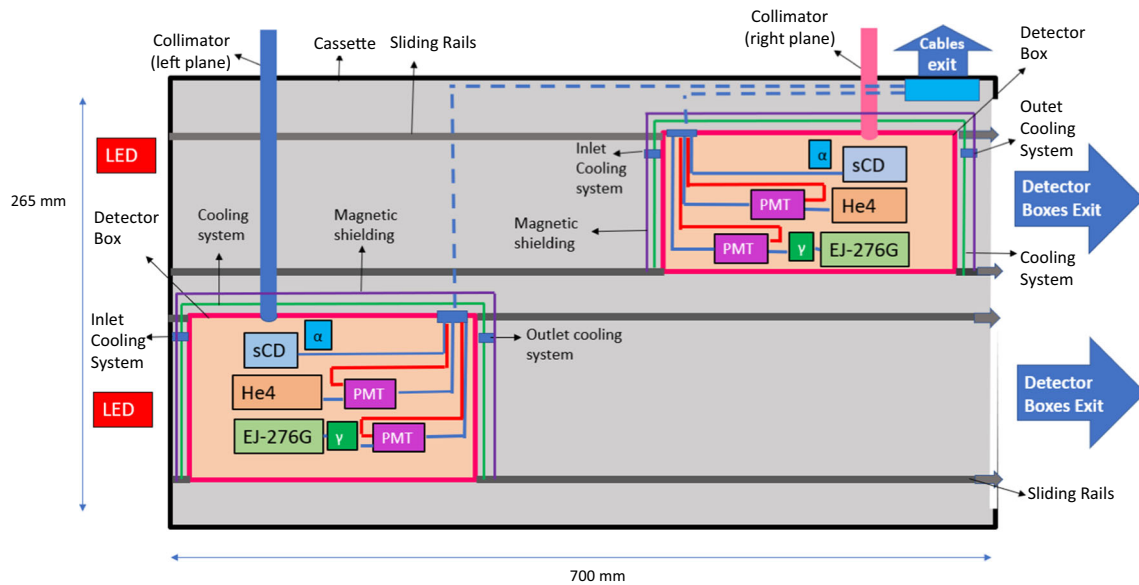


Fig. 7 Ex-Port RNC detectors: schematic view of two Detector Modules for two adjacent LoS

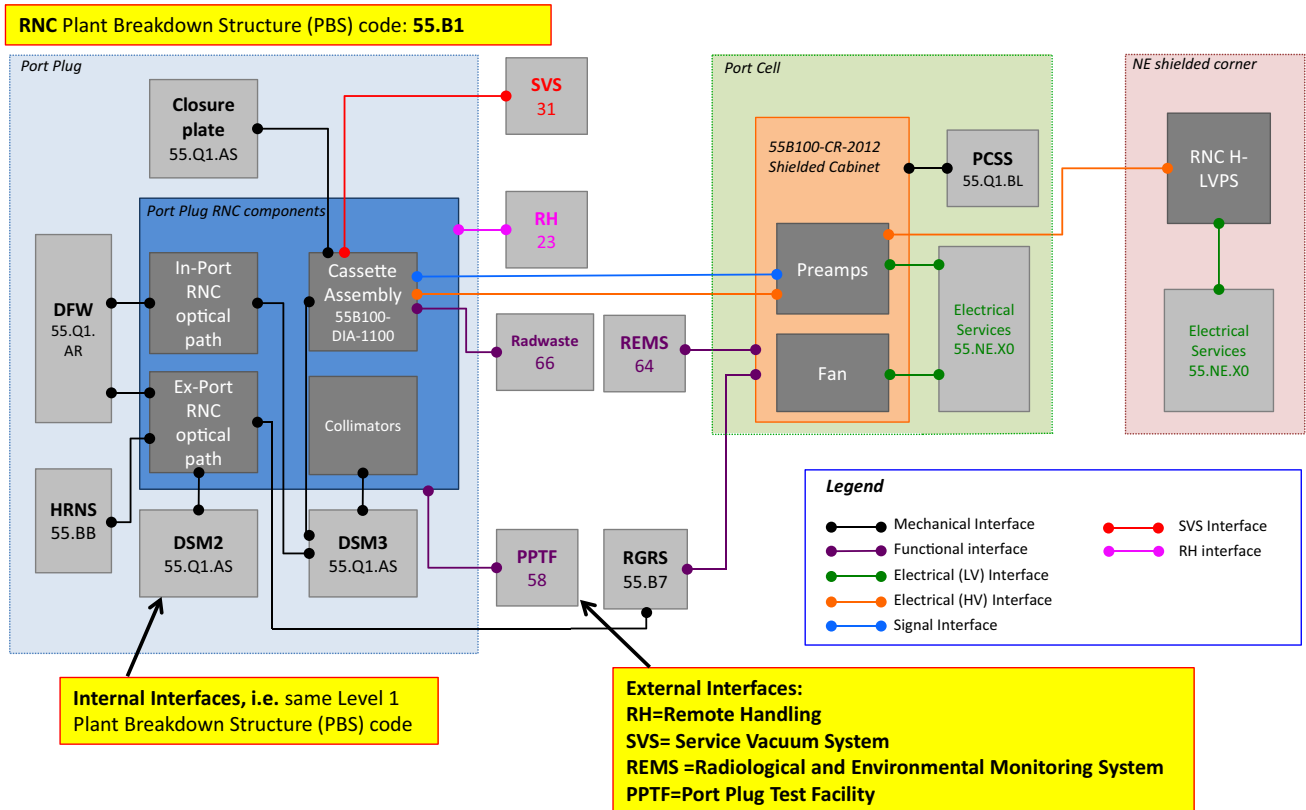


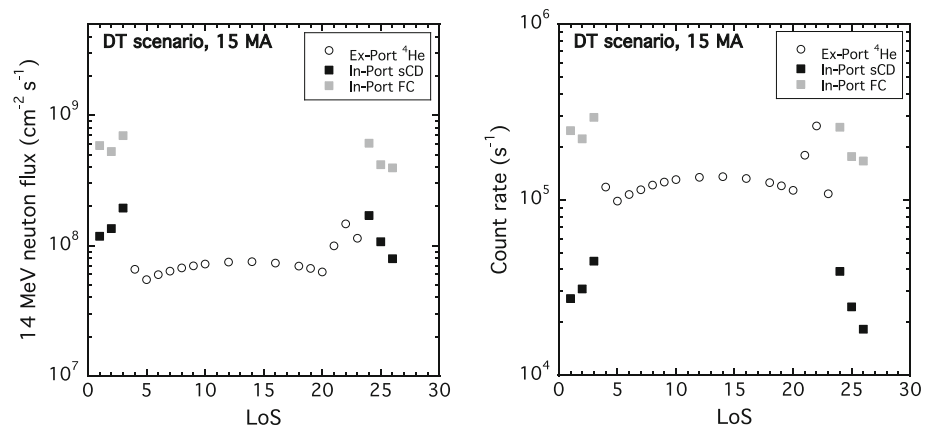
Fig. 8 Interfaces of In-Port RNC

background and statistical uncertainties and assuming a random Gaussian noise with 10% amplitude as uncertainty for the total neutron yield.

Figure 10 (top) shows the results of the performance analysis, in terms of emissivity reconstruction and relative

accuracy, obtained using the MFR method. Clear improvements in the 2D reconstruction of the neutron emissivity are obtained using the total neutron yield constraint [14]: extension of the spatial region in which the accuracy of the reconstruction is < 10%, better

Fig. 9 Neutron fluxes at RNC detectors (left) and count rates (right) above the energy thresholds indicated in Table 1. Fluxes take into account the position of the detectors as well as of the attenuation due to stainless steel structures along the lines of sight; count rates take into account of the actual sensitive area of the detectors



reconstruction of peaked emissivity profiles and robustness against measurements noise/loss of LoS data. The consistency of the two different analysis methods is shown in Fig. 10 (bottom) that compares the accuracy provided by MFR and MSST.

A further step in the evaluation of the RNC performance is the real-time implementation of the RNC acquisition and processing algorithms in order to validate the measurement requirements. For this implementation the 1D reconstruction based on Tikhonov regularization (MSST code) was used. The real-time algorithms calculating the RNC neutron emissivity profile are assumed to be divided in 3 distinct tasks that must run (control cycle time) within the time requirement for emissivity reconstruction (10 ms): (1) Acquisition of RNC measurements and provision of the line-integrated signal for each LoS; (2) Retrieval of the equilibrium data and provision of the intersections of each LoS with a pre-defined set of magnetic surfaces; (3) Calculation of the neutron emissivity profile using the inputs from the previous tasks and the 1D inversion algorithm.

A test and development prototype software and hardware was used with the following specifications:

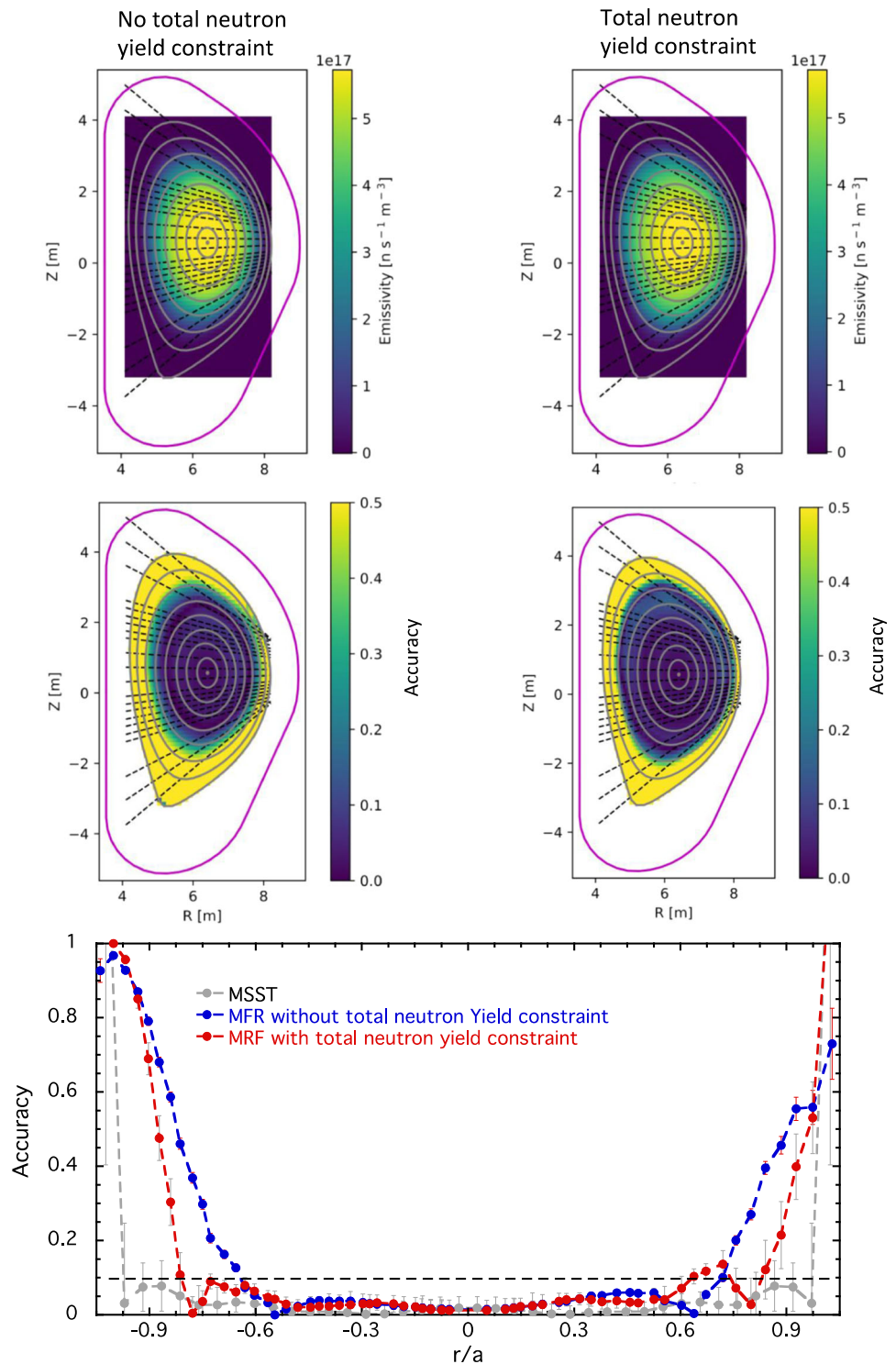
- Real-time operating system: Scientific Linux 7.0 with Real Time kernel.
- In-house developed device drivers.
- Host personal computer (PC) running on Intel® Core™ i7-5930 K CPU at 3.50 GHz with 6 cores and 12 independent software threads, 64-GB memory, and 256-GB solid state drive.
- Xilinx KC705 evaluation board featuring a Kintex 7 field programmable gate array (FPGA).
- In-house developed firmware featuring analog-to-digital converter (ADC) readout, PCIe direct memory access data streaming management, event detection, and pulse analysis.
- In-house developed analog input with 2 ADC 12-bit at up to 1.6-GHz FPGA Mezzanine Card.

The real-time implementation of task 1 was performed both on the FPGA and on the Host PC. In both options the pulse processing algorithm performs the following main functions: baseline evaluation, saturation detection, pile-up detection, signal integration (energy calculation), neutron/gamma separation, construction of energy spectrum per particle, count rate calculation. The processing time of the two hardware options has been evaluated by feeding emulated n and γ pulses (CAEN DT5800D two-channel pulse signal emulator) into the analog input of the FPGA Mezzanine Card and subsequently processing them either by the FPGA or the Host PC. Since all FPGA code is implemented in HDL, with no embedded software processors included, the overall expected latency introduced by the processing modules in the FPGA is within 0.2 ms. The processing times in the Host PC are longer and count rate dependent: using one CPU core with 10-ms control cycle, the pulse processing algorithm runs in 12 ms for a peak event rate of $2.0 \times 10^6 \text{ s}^{-1}$ and $< 10 \text{ ms}$ for event rates up to $1.5 \times 10^6 \text{ s}^{-1}$.

The real-time implementation of tasks 2 and 3 was carried out on the Host PC using the Multithreaded Application Real-Time executor (MARTe, [15]), a multiplatform open source framework widely used in fusion experiments. Two separate MARTe Generic Application Modules have been developed to perform tasks 2 and 3 and their performances evaluated for various ITER plasma scenarios considering line-integrated input data (b) with different random noise level (1%, 3%, 12%) and 20 magnetic surfaces for the reconstruction. Figure 11 summarizes the results of the analysis for the reference case of the DT Q = 10 scenario showing that the tasks 2 and 3 run always in less than 1.5 ms.

In summary, it was demonstrated [16–20] that the acquisition and processing phases leading to neutron emissivity reconstruction can be carried out respectively in 0.2 ms and 1.5 ms (total time $< < 10 \text{ ms}$) thus matching the 10 ms real-time measurement requirement. Note that

Fig. 10 2D maps of MFR reconstructed neutron emissivity (top) and associated accuracy (center), with and without inclusion of total neutron yield constraint. Comparison of 1D neutron emissivity reconstruction accuracy with 1σ uncertainty provided by MFR and MSST (bottom)



the time resolution requirement for measurements not to be provided in real-time (1 ms) is, anyway, achievable thanks to the use in the RNC of digital acquisition systems (see e.g.: [21]).

Table 2 summarizes the ITER scenarios used in the RNC performance analysis simulations. The associated

achievable performances are provided in Table 3: the profile regions (in terms of r/a range and associated emissivity) in which such performances are achievable in real-time simultaneously are also indicated. The table is based on MSST 1D simulations that include direct uncertainty (Poisson statistical uncertainty, background due to

Fig. 11 Real-time neutron emissivity reconstruction in for the DT Q = 10 scenario at different levels of random noise using 20 magnetic surfaces

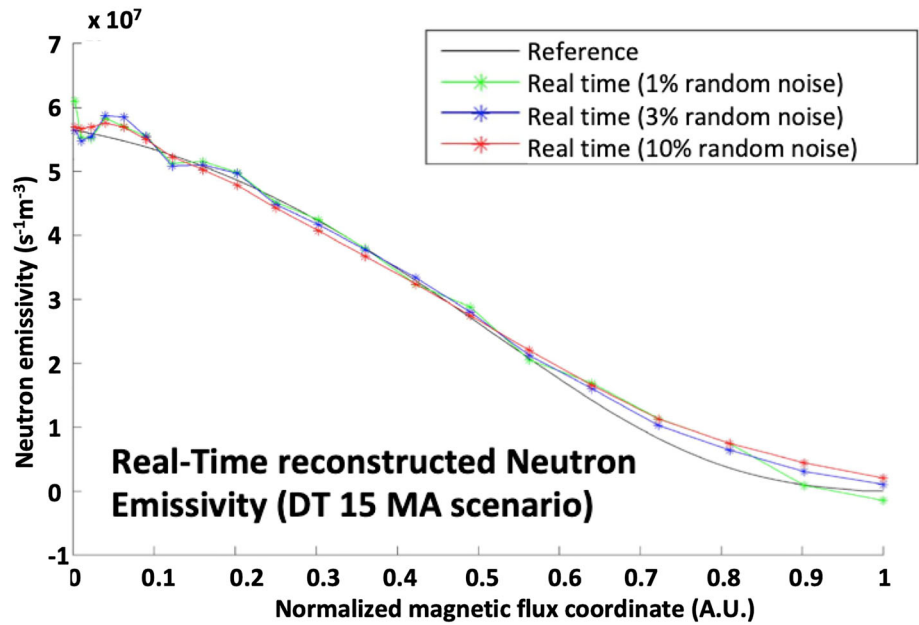


Table 2 ITER scenarios used in the RNC performance analysis

#	Scenario	Code	Ip (MA)	B (T)	Fuel	Fusion power (MW)	Peak neutron emissivity (s ⁻¹ m ⁻³)	Neutron yield (s ⁻¹)
1	DT_17MA	17 MA	17	5.3	DT	700	1.1 × 10 ¹⁸	2.6 × 10 ²⁰
2	Plasma_Data_15_MA_-_4.5_KeV-Corsica_467GXM_v1_0	DT Q = 10	15	5.3	DT	500	5.7 × 10 ¹⁷	1.8 × 10 ²⁰
3	DT-15MA-FlatN-Q = 5	DT Q = 5	15	5.3	DT	255	3.7 × 10 ¹⁷	9.8 × 10 ¹⁹
4	DT_Half-B_H (nt = 0.76ne)	DT LOW	7.5	2.65	DT	23	4.9 × 10 ¹⁶	8.4 × 10 ¹⁸
5	DD_Full-B_H (0.28nG)	DD HIGH	15	5.3	DD	1	3.1 × 10 ¹⁵	1 × 10 ¹⁸

Table 3 Summary of RNC performance for neutron emissivity profile measurements (real-time)

Scenario #	Neutron emissivity range (s ⁻¹ m ⁻³)	Time resolution (ms)	Accuracy (%)	Spatial resolution	r/a
DT Q = 10	1.4 × 10 ¹⁷ –5.7 × 10 ¹⁷	10	10	a/10	< 0.8
DT Q = 5	2.2 × 10 ¹⁷ –3.6x10 ¹⁷	10	10	a/10	0.15–0.5
DT LOW	9.6 × 10 ¹⁵ –4 × 10 ¹⁶	100	10	a/10	0.2–0.65
DD HIGH	1.5 × 10 ¹⁵ –3.8 × 10 ¹⁵	100	20	a/10	< 0.6

scattered neutrons, random noise on acquired detector pulses, attenuation, detector efficiency, etendue) and indirect uncertainty (equilibrium reconstruction).

R&D and Prototyping Testing

The R&D and Prototype Testing activity has focused on the following issues:

- a) verification of the resistance of sCD and ²³⁸U FC detectors to the environmental/operational conditions expected in the In–Port RNC (Sect. 4.1);
- b) manufacturing and test of the In–Port RNC electrical feedthrough (Sect. 4.2);
- c) assessment of the Electro Magnetic Compatibility of the Front–End Electronics (Sect. 4.3);
- d) manufacturing and test of a novel pressurized ⁴He scintillator detector for the Ex–Port RNC (Sect. 4.4).

Resistance of sCD Matrix and ^{238}U Fission Chamber to Environmental Conditions

The main issues concerning the operation of sCD in the In-Port RNC are related to the resistance to high temperature, gamma radiation and 14 MeV neutron fluence, while the main concern for the FC is the operation at high count rate. Prototype sCD and FC have been built (Fig. 12) and tests have been carried out at experimental facilities as described in the following subsections.

sCD Thermal Fatigue Tests

During the ITER baking process the components within the Cassette containing the In-Port RNC detectors are required to withstand 200 °C. Tests have been carried out to check whether the sCD matrix prototype can withstand the foreseen baking periods (500 baking cycles accommodate from the commissioning phase to the end of life of ITER) without any need of additional cooling. An accelerated test procedure has been developed and a dedicated thermal test facility has been built at IFJPAN (Krakow, Poland) to simulate baking cycles in dark and no bias voltage testing environment [22]. The features of these tests (*Temperature Cycling Test (TCT)* and *Steady Temperature Test (STT)*) are sketched in Fig. 13. The STT and TCT carried out on the sCD matrix detector prototype have covered

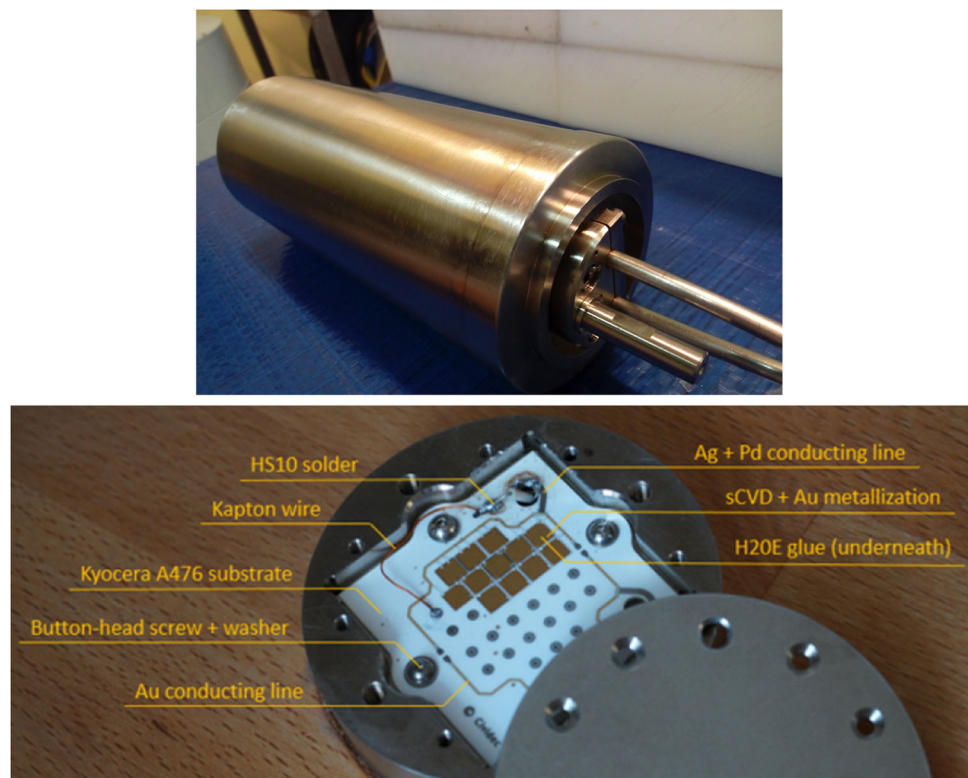
respectively $\sim 73\%$ of baking time at maximum temperature and 2.5 times the number of baking cycles expected during ITER DT pulse operation. The flat top temperature of STT test is 200 °C and the TCT test has been performed between 100 and 200 °C with a ramp-up/ramp-down rate of 40 °C/h (8 times faster than the 5 °C/h rate expected in ITER) (Fig. 14). The parameters monitored during the execution of the tests are the position and the Full Width Half Maximum (FWHM) of the emission lines of a $^{239}\text{Pu}/^{241}\text{Am}/^{244}\text{Cm}$ tri-alpha source; all measurements have been carried out at 100 °C. Observed variations of the monitored parameters are within the acceptance criteria set for the test: shift of the position of the alpha peaks $< 5\%$ (with no drift), variation of the FWHM of the alpha peaks $< 5\%$ (Fig. 14). Based on these results, it was decided that no cooling system is needed for the sCD in the In-Port RNC.

sCD Gamma Radiation Hardness

Gamma irradiation tests were carried out on sCD detectors to check the resistance of these detectors to the gamma dose expected at ITER end life, which according to MCNP simulations is 5.6 MGy [23].

The experiments were carried out on three identical commercial sCD diamond detectors (size: 4.5 mm 4.5 mm, thickness: 500 μm , Ti-carbide/Ag contact) at the

Fig. 12 Detector prototypes: ^{238}U fission chamber manufactured by Centronic (top) and sCD Matrix (bottom)



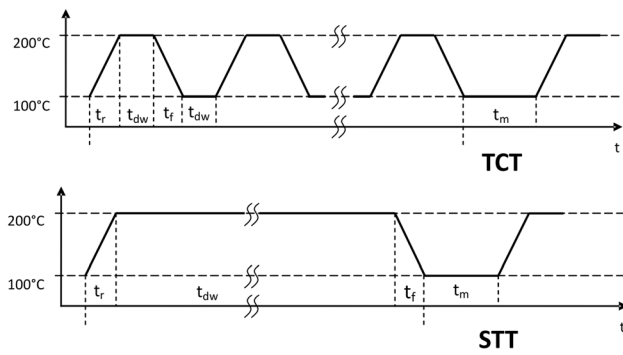


Fig. 13 Details of the Temperature Cycling Test (top) and of the Steady State Test (bottom): t_r = temperature ramp-up time, t_f = temperature ramp-down time, t_m = time of measurement with alpha source, t_{dw} = dwell time

CALLIOPE facility (ENEA-Casaccia) with a ^{60}Co source in an air and room temperature testing environment with two dose rates (1.4 kGy/h and 0.3 kGy/h). Negligible effects were experienced in the sCD count rates [22, 24] up to 3 MGy, while deterioration was found for higher doses.

Based on this result, the present design of the sCD detector in the In-Port RNC includes a 2.5 mm thick tungsten coating deposited (using the Plasma Spray technique) on the outer surface of the detector holder: such coating reduces the gamma dose at ITER end life to about 3 MGy.

sCD Neutron Radiation Hardness

Three commercially available sCD, respectively 100, 300 and 500 μm thick (size: 0.2 mm 0.2 mm), with identical contact technology (Ti-Ag), were irradiated simultaneously at increasing steps of 14 MeV neutron fluence up to $3.98 \times 10^{14} \text{ cm}^{-2}$ at flux levels ($2 \times 10^9 \text{ s}^{-1} \text{ cm}^{-2}$) comparable to those expected in ITER [25]. The aim was the selection of the best sCD thickness as a trade-off between efficiency and minimization of neutron radiation damage.

After each irradiation step, a pulse height spectrum was measured for the irradiation of the detector with 14 MeV neutrons, which was recalibrated using ^{241}Am alpha source measurements. The net result is a decrease of the Charge

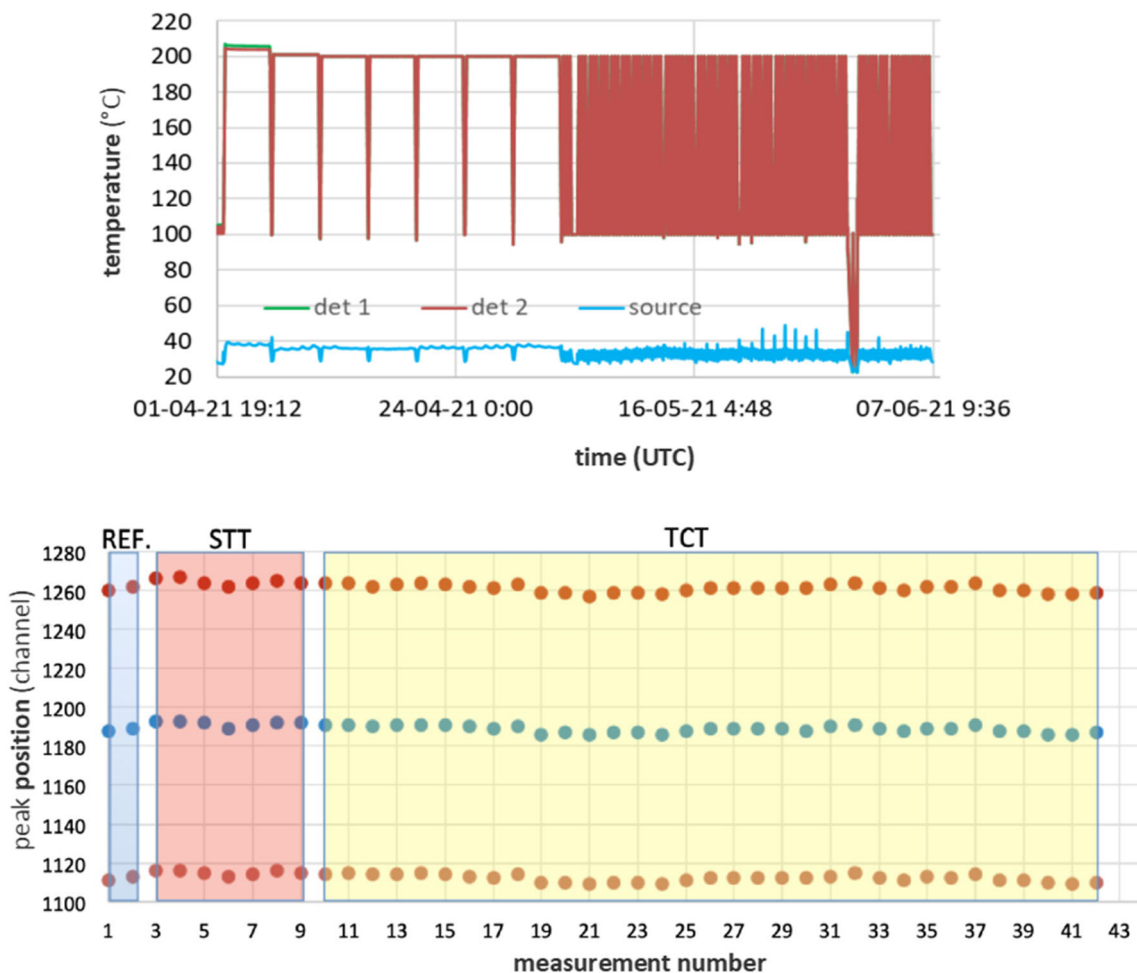


Fig. 14 Measured temperature (top) and alpha source peak position (bottom) during the thermal fatigue tests of the sCD prototype

Collection Efficiency with increasing fluence for any given detector thickness, as shown by the shift of the 14 MeV peak towards lower energies. A clear polarization effect is observed (especially after the last irradiation steps) and depends on the duration of the acquisition: the peak shift increases with the charge accumulated in the detector. The results indicate a lower degradation of detector performances for thinner sCD, with the 100 μm thick detector being the best performing.

An estimation of the radiation hardness of a 50 μm thick sCD has been made extrapolating the experimental results (including a software polarization correction). The method is based on the fitting of the polarization corrected charge collection efficiency as a function of the fluence with a simple quadratic curve. It is predicted that a 50 μm thick sCD detector can withstand a 14 MeV neutron fluence of the order of $1.0 \times 10^{15} \text{ cm}^{-2}$ with a *Charge Collection Efficiency* reduction to about 0.7, i.e. the value at which the polarization correction algorithm fails. Based on these results, a 50 μm thick sCD has been selected for the In-Port system.

The expected neutron fluence at these detectors at the end of ITER life is $\sim 1 \times 10^{16} \text{ cm}^{-2}$, while based on the results above, the sCD matrix will experience degradation at a fluence value one order of magnitude below. Therefore the sCD will be used, before its full degradation, to properly cross calibrate these detectors with the FC, which, on the contrary, can withstand the fluence expected at the end of ITER life and will replace the sCD after their failure without major impacts on the diagnostic performance.

FC High Count Rate Operation

The objective of this test is to assess the linearity of the ^{238}U FC prototype count rate with 14 MeV neutron flux. In the ITER DT Q = 10 scenario $\sim 1.5 \times 10^9 \text{ s}^{-1} \text{ cm}^{-2}$ are impinging on the ^{238}U FC and the expected count rate is $\sim 4 \times 10^5 \text{ s}^{-1}$. An experiment was carried out at the Frascati Neutron Generator (FNG) facility in which the ^{238}U FC prototype was irradiated with 14 MeV neutrons up to the maximum achievable count rate. A good linearity of the FC count rate versus the calibrated α particle count rate (silicon detector installed inside the beam line) was measured for a FC count rate up to $8 \times 10^4 \text{ s}^{-1}$ (Fig. 15). Pile-up was detected at the higher count rates values (maximum measured fraction of 15%), but it was handled with no problem by the digital acquisition and processing algorithm [21].

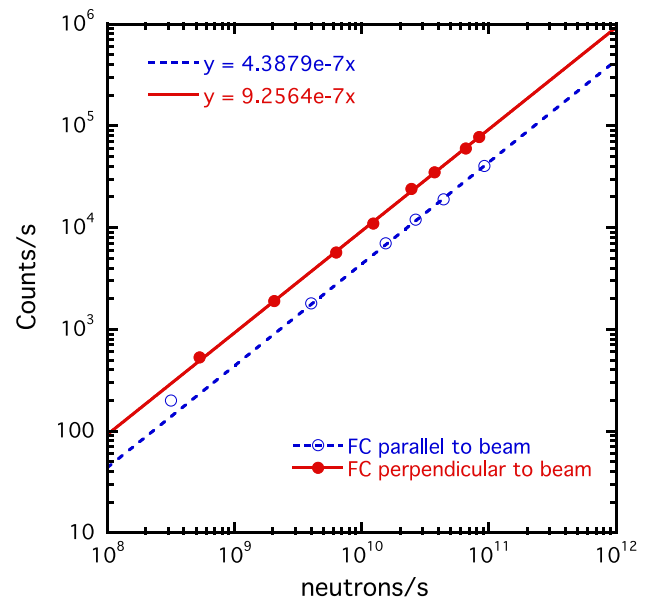


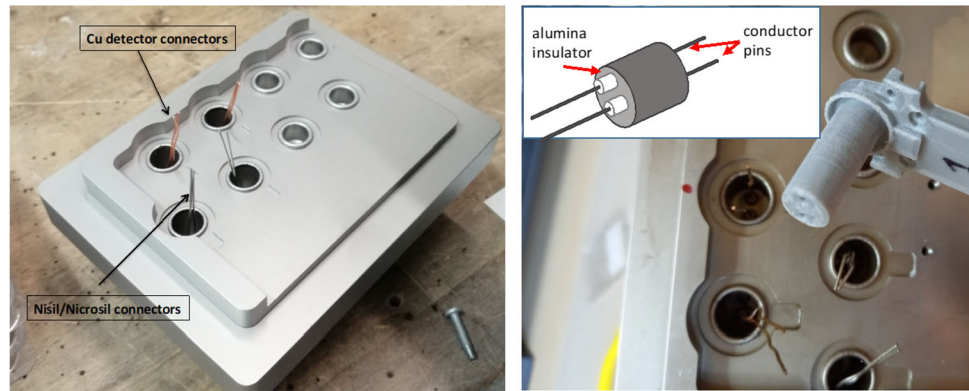
Fig. 15 Linearity of ^{238}U fission chamber count rate with 14 MeV neutrons

Manufacturing and Test of the In-Port RNC Electrical Feedthrough

A prototype of the *Electrical Feedthrough* installed at the boundary between the ITER primary vacuum and the secondary vacuum inside the In-Port RNC cassette assembly was manufactured (Fig. 16) and tested. The aim is to demonstrate its manufacturability and assembly, to verify the structural properties and the requirements related to the confinement function after assembly operations (welding) and under environmental, operational and accidental loads and to verify the electrical performances in terms of insulation and conduction both after manufacturing/assembly and after thermal and structural tests. The *Electrical Feedthrough* prototype is equipped with four connectors manufactured by Ceramtec: two detector cables connectors (Copper) and two Thermocouples connectors (Nisil-Nicrosil).

Non-destructive test examination of welding between plate and connectors and of brazing between pins and ceramic insulators (radiographic inspection), helium leak test, electrical performances (insulation and conduction) test, thermal vacuum cycling test, pressure cycle test and vibration tests were carried out. All tests were passed successfully, also showing that the prototype does not introduce significant distortion or attenuation of the detector signals.

Fig. 16 Electrical feedthrough prototype



Electro Magnetic Compatibility of the Front-End Electronics

The following potential *Electro Magnetic Compatibility* issues have been identified for the front-end electronics: immunity to static, fluctuating and radiated field, immunity to conducted disturbances on signal and power ports (both *Common and Differential Mode* noise, in the form of surges, fast transients or continuous waves), immunity to radiated disturbances, immunity to direct and indirect *Electrostatic Discharge*, conducted and radiated emissions.

These issues have been studied by means of the design, construction and characterization of a mock-up system for RNC fast signal chains (neutron detector signal) and slow signal chains (thermocouple signal—for detector temperature monitoring). Figure 17 shows the fast signal mock-up composed by a pulse source, emulating the electrical signal emitted by a 100 μm thick sCD matrix detector with a total electrical capacitance of 225 pF, a prototype of the cassette electrical feedthrough (secondary/primary vacuum interface), a metal box emulating the electrical feedthrough on the closure plate (primary vacuum/air interface), a stage of signal conditioning and amplification (which is

representing the electronics inside the shielded cabinet), and a final stage for the signal acquisition.

This system passed all the applicable *Electro Magnetic Compatibility* tests, according to the general requirements imposed by the norms for kind of systems, and to the additional requirements imposed by ITER guidelines [26]. The tests were carried out at the EMCLab facility of the University of Cassino and Southern Lazio, part of the CREATE Consortium. In particular, the following components are found to be required to guarantee the *Electro Magnetic Compatibility* compliance: (1) in the shielded cabinet: transient voltage suppressors at all the connectors of the signal chains, common mode chokes and ferrite filters in the high voltage and low voltage circuits; Electro Magnetic Interference filter in the low voltage circuit; inductive filter at the amplifier output circuit; (2) in the acquisition stage: transient voltage suppressors at the input of the stage, LAN transformer.

^4He Scintillator

Liquid scintillators such as NE213 or BC501 have been routinely used in neutron cameras in tokamaks, e.g.: at JET [27], but they pose significant safety issues due to flammability. An alternative approach based on a ^4He gas scintillator has been adopted for the Ex-Port RNC, where this type of detectors will be primarily used the full power DT measurements. A prototype ^4He gas scintillator composed of an ultra-clean high-pressure gas in a stainless steel tube was developed and tested in dedicated experiments at PTB [28]. The active volume is filled with ^4He scintillating gas at a pressure of ~ 150 bar, doped with a special mixture of noble gas(es) in order to have pulses of 500 ns pulse length. A full neutron detection characterization was performed with mono-energetic neutrons (1.5 MeV, 2.5 MeV, 3.2 MeV, 7.2 MeV and 14.8 MeV) and it was shown that there is a linear relationship between the incident neutron energy and the maximum light output, indicating that this ^4He detector is capable of preserving the

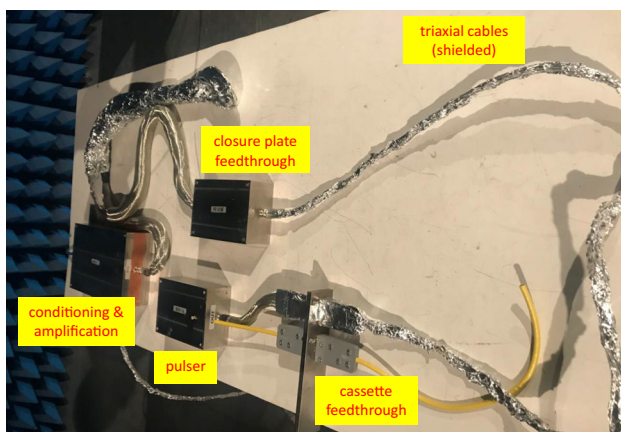
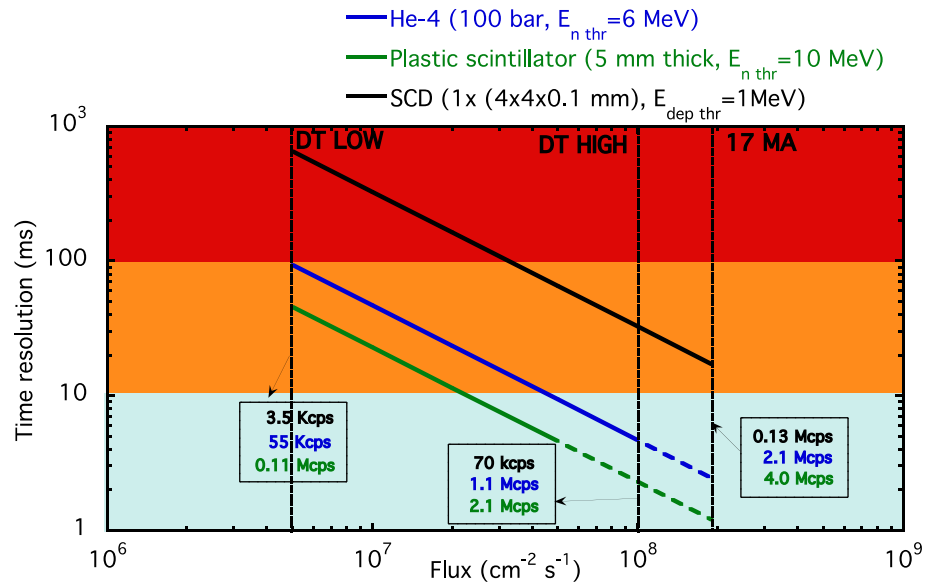


Fig. 17 Front-end electronics fast signal mock-up

Fig. 18 Neutron emissivity reconstruction achievable with Ex-Port RNC detectors. Dashed lines correspond to ranges in which the total count rate (no energy threshold) exceeds 1 Mcps. Count rates shown are indicated for each detector at fluxes corresponding to DT LOW, DT HIGH and 17 MA scenario



information about the incident neutron energy. The prototype was also characterized in collimated-beam conditions similar to those expected for the RNC. The response function to 2.5 MeV and 14.8 MeV neutrons was measured and validated by Monte Carlo simulations. Complete gamma rejection is achieved through pulse height analysis by setting a threshold of 0.30 MeV in terms of deposited energy, which corresponds to an energy of 0.45 MeV in terms of incident neutron energy. Based on the results on this prototype, a second prototype (100 bar, length = 30 mm, diameter 44 mm) is being constructed with the aim of solving some integration and engineering issues and of optimizing the efficiency. The ^4He detector, used in combination with the plastic scintillator and the sCD detector, will enable to cover the neutron emissivity dynamic range at the required time resolution (see Fig. 18).

Conclusions and Prospects for the RNC Procurement

The paper provides a review of the progress and development carried out on the design of the ITER Radial Neutron Camera. The status of the design is presented at the stage in the ITER procurement process when the In-Port RNC subsystem has undergone the Final Design Review and the Ex-Port RNC subsystem is in preparation for the Preliminary Design Review.

The main results of the program of prototyping and testing supporting the most critical issues of the RNC diagnostic design are described.

For the In-Port system: (a) prototypes of the neutron detectors (single Crystal Diamond matrix and ^{238}U fission chamber) were manufactured and tested for the assessment

of the final design choices and, in particular, neutron/gamma irradiation and thermal fatigue tests at 200 °C of the single Crystal Diamond matrix led, respectively, to the choice of most suitable detector thickness (50 μm) and to the result of a great simplification of the design by avoiding the need of the detector cooling system; (b) the design of the electrical feedthrough at the vacuum interface was validated by the construction and extensive tests of a prototype; (c) the electromagnetic compatibility issues of the front-end electronic chain were studied and assessed through the construction and test of a mock-up.

For the Ex-Port system: a prototype ^4He gas scintillator was developed and tested with monoenergetic neutrons confirming the suitability for DT full power measurements. The detector features a linear relationship between the incident neutron energy and the maximum light output and the capability of gamma rejection by use of through pulse height analysis. The construction of a second prototype is in progress as a basis for the final design.

The performance of the RNC in terms of neutron emissivity measurement capability was assessed through 1D and 2D reconstruction analysis. It was proven that the neutron emissivity can be reconstructed in real-time within the measurement requirements: 10% accuracy, 10 ms time resolution and $a/10$ (a = plasma minor radius) space resolution.

The construction of the RNC is proceeding according to schedule, with the In-Port system expected to be delivered must be delivered to ITER Organization by end 2025 and the Ex-Port system ready for delivery in 2030.

Acknowledgements The work leading to this publication has been partially funded by Fusion for Energy under the Specific Grant Agreement F4E-FPA-327 (Specific Contracts 01, 02, 03, 05, 06 and 07). The sCD matrix prototypes have been produced under F4E-OPE-

1001 and the fission chamber prototype under F4E-OPE-0954. This scientific work is published as part of an international project co-financed by the Polish minister of Science and Higher Education, entitled “PMW” in the years 2020-2024, within the framework of the scientific financial resources for 2021 under the contract numbers 5133/ITER/2020/0 and 111/ITER/2020/0.

Open Access This article is licensed under a Creative Commons Attribution 4.0 International License, which permits use, sharing, adaptation, distribution and reproduction in any medium or format, as long as you give appropriate credit to the original author(s) and the source, provide a link to the Creative Commons licence, and indicate if changes were made. The images or other third party material in this article are included in the article’s Creative Commons licence, unless indicated otherwise in a credit line to the material. If material is not included in the article’s Creative Commons licence and your intended use is not permitted by statutory regulation or exceeds the permitted use, you will need to obtain permission directly from the copyright holder. To view a copy of this licence, visit <http://creativecommons.org/licenses/by/4.0/>.

Funding Open access funding provided by Ente per le Nuove Tecnologie, l’Energia e l’Ambiente within the CRUI-CARE Agreement.

Data Availability The datasets generated during and/or analysed during the current study are available from the corresponding author on reasonable request.

References

- Bertalot et al., Present status of ITER neutron diagnostics development. *J. Fusion Energ.* **38**, 283 (2019)
- M. Sasao et al., Chapter 9 fusion product diagnostics. *Fusion Sci. Technol.* **53**, 604 (2008)
- D. Marocco, B. Esposito, F. Moro et al., System level design and performances of the ITER radial neutron camera, in *FIP 524 Proceedings of the 26th IAEA Fusion Energy Conference*, 4–16 (2016)
- R. Rodionov et al., Optimization of the ITER vertical neutron camera detectors and collimators. *Fusion Eng. Des.* **166**, 112341 (2021)
- D. Dongiovanni et al., Design space exploration for architecture selection: radial neutron camera nuclear fusion diagnostic study case. *Fusion Eng. Des.* **137**, 378 (2018)
- F. Moro et al., The ITER radial neutron camera in-port system: nuclear analyses in support of its design development. *Fusion Eng. Des.* **146**, 236 (2019)
- M. Ceconello et al., Strategy and guidelines for the calibration of the ITER radial neutron camera. *Fusion Eng. Des.* **146B**, 2049 (2019)
- M. Scholz et al., Conceptual design of the high resolution neutron spectrometer for ITER. *Nucl. Fusion* **59**, 065001 (2019)
- M. Nocente, M. Tardocchi et al., Conceptual design of the radial gamma ray spectrometer system for a particle and runaway electron measurements at ITER. *Nucl. Fusion* **57**, 076016 (2017)
- C. Centioli et al., Interface definition and integration in the equatorial port 01 of the ITER In-port radial neutron camera. *Fusion Eng. Des.* **172**, 112749 (2021)
- D. Marocco et al., Combined unfolding and spatial inversion of neutron camera measurements for ion temperature profile determination in ITER. *Nucl. Fusion* **51**, 053011 (2011)
- D. Marocco et al., Neutron measurements in ITER using the radial neutron camera. *J. Instrum.* **7**, C03033 (2012)
- M. Odstrcil et al., Modern numerical methods for plasma tomography optimisation. *Nucl. Instrum. Methods Phys. Res.* **A686**, 156 (2012)
- K. Mikszuta-Michalika et al., A total neutron yield constraint implemented to the RNC emissivity reconstruction on ITER tokamak. *Fusion Eng. Des.* **160**, 111840 (2020)
- A. Neto et al., A survey of recent MARTE based systems. *IEEE Trans. Nucl. Sci.* **58**, 1 (2011)
- R. Costa-Pereira et al., Real-time data acquisition prototype proposal of the ITER radial neutron camera and gamma-ray spectrometer. *Fusion Eng. Des.* **123**, 901 (2017)
- N. Cruz, B. Santos et al., The design and performance of the real time software architecture for the ITER radial neutron camera. *IEEE Trans. Nucl. Sci.* **66**(7), 1310 (2019)
- A. Fernandes et al., FPGA code for the data acquisition and real-time processing prototype of the ITER radial neutron camera. *IEEE Trans. Nucl. Sci.* **66**(7), 1318 (2019)
- B. Santos et al., Real-time data compression for data acquisition systems applied to the ITER radial neutron camera. *IEEE Trans. Nucl. Sci.* **66**(7), 1324 (2019)
- B. Santos et al., Linux device driver for radial neutron camera in view of ITER long pulses with variable data throughput. *Fusion Eng. Des.* **146B**, 1698–1702 (2019)
- M. Riva et al., Hardware architecture of the data acquisition and processing system for the JET neutron camera upgrade (NCU) project. *Fusion Eng. Des.* **123**, 873 (2017)
- F. Pompili et al., Radiation and thermal stress test on diamond detectors for the radial neutron camera of ITER. *Nuclear Inst. Methods Phys. Res.* **A936**, 62 (2019)
- M. Riva et al., High-priority prototype testing in support of system-level design development of the ITER radial neutron camera. *IEEE Trans. Plasma Sci.* **46**, 1291 (2018)
- S. Baccaro et al., Radiation damage tests on diamond and scintillation detector components for the ITER radial neutron camera. *IEEE Trans. Nucl. Sci.* **65**(8), 2046 (2018)
- M. Passeri et al., Assessment of single crystal diamond detector radiation hardness to 14 MeV neutrons. *Nuclear Inst. Methods Phys. Res.* **A1010**, 165574 (2021)
- A. Maffucci et al., EMC Issues and Signal Integrity Analysis of Neutron Diagnostics for Nuclear Fusion Machines, in *Proceedings of the IEEE 26th Workshop on Signal and Power Integrity (IEEE SPI)*, Siegen, Germany, 22–25 May, 2022, paper ID #50
- M. Adams et al., The JET neutron emission profile monitor. *Nuclear Inst. Methods Phys. Res.* **A329**, 277–290 (1993)
- Q. Ducasse et al., Characterization of the response and the intrinsic efficiency of a ^4He scintillation detector to fast mono-energetic neutrons. *Nuclear Inst. Methods Phys. Res.* **A998**, 165168 (2021)

Publisher’s Note Springer Nature remains neutral with regard to jurisdictional claims in published maps and institutional affiliations.

Authors and Affiliations

B. Esposito¹  · D. Marocco¹ · G. Gandolfo¹ · F. Belli¹ · L. Bertalot¹² · J. Blocki² · D. Bocian² · G. Brolatti¹ · M. Ceconello⁸ · C. Centioli¹ · R. C. Pereira⁷ · S. Conroy⁸ · F. Crescenzi¹ · N. Cruz⁷ · L. de Bilbao¹⁰ · A. Domenicone¹ · Q. Ducasse¹⁷ · G. Di Mambro^{4,15} · D. Dongiovanni¹ · I. Eletxigerra¹¹ · B. Etxeita¹¹ · A. Fernandez⁷ · O. Ficker⁹ · P. Gallina¹³ · T. Giacomini¹² · G. Ginoulhiac¹ · J. Godlewski² · A. Hjalmarsson⁸ · M. Imrisek⁹ · R. Kantor² · K. Kasprzak² · J. Kotula² · V. Krasilnikov¹² · M. Lewandowska² · A. Maffucci^{4,15} · U. Marotta¹ · D. Marzullo¹³ · G. Mazzitelli¹ · G. Mazzone¹ · R. Miklaszewski⁶ · K. Mikszuta-Michalik⁶ · W. Maciocha² · S. Magagnino¹ · M. Misano¹ · J. Mlynar⁹ · C. Monti¹ · F. Moro¹ · R. Ortwein² · M. Passeri^{1,5} · T. Pinna¹ · E. Pirovano³ · V. Pisciotta¹ · F. Pompili¹ · S. Podda¹ · M. Riva¹ · B. Santos⁷ · J. Sousa⁷ · J. Swierblewski² · P. Szklarz² · A. Tati¹⁴ · S. Ventre^{4,15} · F. Villone^{4,16} · N. Virgili¹ · A. Zimbal³

✉ B. Esposito
basilio.esposito@enea.it

¹ Fusion and Technology for Nuclear Safety and Security Department, ENEA, C.R. Frascati, Via E. Fermi 45, 00044 Frascati, Rome, Italy

² Institute of Nuclear Physics Polish Academy of Sciences, Radzikowskiego 152, 31342 Kraków, Poland

³ Physikalisch-Technische Bundesanstalt, Bundesallee 100, 38116 Braunschweig, Germany

⁴ Consorzio CREATE, Via Claudio, 21, 80125 Naples, Italy

⁵ Dipartimento di Ing. Civile ed Ing. Informatica, Università di Roma Tor Vergata, Rome, Italy

⁶ Institute of Plasma Physics and Laser Microfusion, Hery Street 23, 01-497 Warsaw, Poland

⁷ Instituto de Plasmas, Fusão Nuclear Instituto Superior Técnico, Universidade de Lisboa, 1049-001 Lisbon, Portugal

⁸ Department of Physics and Astronomy, Uppsala University, 751 05 Uppsala, Sweden

⁹ Institute of Plasma Physics of CAS, Za Slovankou 1782/3182 00, Prague 8, Libeň, Czech Republic

¹⁰ AVS Added Value Solutions, Pol. Ind. Sigma Xixilion Kalea 2, Bajo Pabellón 10 20870 Elgoiba, Gipuzkoa, Spain

¹¹ IDOM, Avenida Zarandoa 23, 48015 Bilbao, Spain

¹² ITER Organization, Route de Vinon-sur-Verdon, 13115 Saint-Paul-lez-Durance, France

¹³ Dipartimento di Ingegneria e Architettura, Università degli Studi di Trieste, Comprensorio di Piazzale Europa 1, 34127 Trieste, Italy

¹⁴ Sustainability Department, Casaccia Research Centre, ENEA, 00123 Rome, Italy

¹⁵ Dipartimento di Ing. Elettrica e dell'Informazione, Università di Cassino e del Lazio Meridionale, 03043 Cassino, Italy

¹⁶ Dipartimento di Ing. Elettrica e delle Tecnologie dell'Informazione, Università di Napoli Federico II, 80125 Napoli, Italy

¹⁷ DES, IRESNE, Nuclear Measurement Laboratory, CEA Cadarache, 13108 Saint-Paul-lez-Durance, France